Materials Science & Engineering A 809 (2021) 140975

Contents lists available at ScienceDirect

Materials Science & Engineering A

journal homepage: http://www.elsevier.com/locate/msea

Interface microstructure and tensile properties of a third generation aluminium-steel butt weld produced using the Hybrid Metal Extrusion & Bonding (HYB) process

Lise Sandnes [a,*], Tina Bergh [b], Øystein Grong [a,c], Randi Holmestad [b], Per Erik Vullum [b,d], Filippo Berto [a]

[a] Department of Mechanical and Industrial Engineering, Norwegian University of Science and Technology (NTNU), Richard Birkelands Vei 2b, 7491 Trondheim, Norway
[b] Department of Physics, NTNU, Høgskoleringen 5, 7491, Trondheim, Norway
[c] HyBond AS, NAPIC, Richard Birkelands Vei 2b, 7491, Trondheim, Norway
[d] Department of Materials and Nanotechnology, SINTEF Industry, Høgskoleringen 5, 7491 Trondheim, Norway

ARTICLE INFO

Keywords:
Hybrid Metal Extrusion & Bonding
Aluminum-steel welding
Tensile testing
Digital image correlation
Intermetallic phases
Transmission electron microscopy

ABSTRACT

The Hybrid Metal Extrusion & Bonding (HYB) process is a patented solid state joining method for metals which utilizes filler material additions to consolidate the weld. In the present investigation the interface microstructure and tensile properties of a 4 mm thick joint, belonging to the third generation Al-steel HYB butt welds, are characterized. The mechanical testing shows that the HYB weld exhibits excellent tensile properties, displaying ultimate tensile strength values in the range from 238 to 266 MPa. Moreover, supplementary digital image correlation analysis of the strain evolution occurring during tensile testing reveals that all plastic deformation is localized to the soft heat-affected zone on the aluminium side of the joint, leading to necking and final fracture in the aluminium. Scanning and transmission electron microscopy examinations of the Al-steel interface show that bonding occurs by a combination of microscale mechanical interlocking and intermetallic compound formation. The intermetallic layer has a thickness varying between 0.1 and 1 μm and is composed of Al–Fe–Si crystals. This makes the butt joint highly resistant against interfacial cracking. The subsequent benchmarking against commercial fusion and solid state welding methods reveals that the tensile properties of the Al-steel HYB weld even surpass those reported for comparable friction stir welds. At the same time, the HYB process allows butt welding to be performed at much higher speeds compared to friction stir welding, without compromising the mechanical integrity of the weldment.

1. Introduction

There is an increasing interest in welding of aluminium (Al) alloys to steel for industrial applications due to the growing demand for weight reduction in engineering design. One of the major challenges in Al-steel welding is the formation of hard and brittle intermetallic compounds (IMCs) along the bonded interfaces [1–5]. The formation and growth of these IMCs depends both on the time and temperature during welding, as well as the presence of constituent elements influencing the reaction kinetics [6–13]. Both the chemical composition, morphology and thickness of the resulting IMC layer affect the mechanical integrity of the joint [12–16]. Although metallurgical bonding between Al and steel occurs via IMC formation, the characteristic high heat inputs normally associated with conventional welding processes result in excessive growth of these phases and thus to a thick IMC layer with low bond strength [12,17,18]. At the same time the high heat inputs lead to the formation of a wide heat-affected zone (HAZ) on the Al side of the joint with degraded properties [5,19,20]. So far, a number of different welding processes have been tried out for joining of Al to steels, including different variants of gas metal arc welding (GMAW) and friction stir welding (FSW) [1,5,17,21–32]. However, because of the imminent risk of interfacial cracking during shear and tensile loading, fabrication of reliable Al-steel welds is challenging. Apparently, only low heat input processes, such as FSW and cold metal transfer welding (CMTW), are capable of producing Al-steel welds suitable for industrial use [33,34].

* Corresponding author.
E-mail address: lise.sandnes@ntnu.no (L. Sandnes).

https://doi.org/10.1016/j.msea.2021.140975
Received 13 October 2020; Received in revised form 8 February 2021; Accepted 13 February 2021
Available online 23 February 2021

The advantage that the solid state FSW process offers compared to fusion welding when it comes to restricting the growth of the IMC layer during Al-steel joining is well documented [2,3]. Recently, a new solid state joining method has been developed, combining favourable features of GMAW and FSW. The invention, which is known as the Hybrid Metal Extrusion & Bonding (HYB) process, utilizes continuous extrusion as a technique to enable Al filler metal (FM) additions during joining [16, 35–41]. Originally, the HYB process was developed for butt welding of Al plates and profiles [40,41], but over the years it has evolved into a versatile joining technique handling a wide range of joint configurations and material combinations [35–39]. In particular, the HYB method has shown a great potential for Al-steel welding [35–37]. This is mainly because of its low process temperature, which restricts the growth of the IMC layer [16]. Recently, transmission electron microscopy (TEM) investigations have revealed evidence of a 10–50 nm thin IMC layer along the interface between Al and steel in a 4 mm thick HYB butt joint exhibiting decent tensile properties [16,42]. The strength achieved is attributed to the combination of nanolayer film formation (composed of Al–Fe–Si crystals) and microscale mechanical interlocking [42].

At present, limited information is available in the literature on the mechanical properties of Al-steel HYB joints. However, in an early study from 2018 ultimate tensile strength (UTS) values in the range of 104–140 MPa were reported for a 4 mm thick butt joint produced using AA6082 as FM [35]. In this first generation of Al-steel HYB butt welds severe root and surface defects strongly affected the fracture behaviour. Hence, the joints produced were unsuitable for industrial use. The second generation Al-steel HYB butt welds showed more promising tensile properties, displaying UTS values typically in the range of 184–221 MPa [42]. In the butt weld referred to, the fracture started from cracks in the root region after significant plastic deformation of the Al. The cracks then propagated along the Al-steel interface until final failure occurred [42]. Recently, a third generation of Al-steel HYB butt welds has been made, characterized by an UTS of about 265 MPa [37]. This strength level is slightly higher than that reported for corresponding FS welds, typically being characterized by UTS values in the range of 200–255 MPa [20,43–49]. In the third generation of Al-steel HYB butt welds fracture occurs no longer by crack propagation along the bonded interface but rather by necking in the soft HAZ on the Al side of the joint. This is the preferred failure mode from a structural integrity point of view.

At present, it is not known which factors that contribute most to the observed shift in the fracture behaviour of the third generation Al-steel HYB welds. Thus, the aim of this work is to characterize its interface microstructure and tensile properties to better understand the mechanisms behind the improved cracking resistance. This will be done by combining optical microscopy, scanning electron microscopy (SEM) and TEM characterizations with hardness measurements and tensile testing. In the latter case also supplementary digital image correlation (DIC) analysis has been carried out to document the strain evolution that occurs within the weld zone during tensile testing. Based on these examinations, valuable insight into the underlying structure-property relationships has been obtained, which sheds new light upon how Al-steel butt welds in general respond to tensile loading.

2. Experimental

The third generation Al-steel HYB butt weld was produced in HyBond's research laboratory at the Norwegian University of Science and Technology (NTNU). The pilot HYB machine at NTNU allows welds to be produced under controlled conditions, with full documentation of all relevant process parameters, e.g. extruder temperature, torque, rotational speed, travel speed and wire feed rate as well as the main reaction forces acting on the extruder during welding. Further details about the pilot HYB machine and how it works can be found elsewhere [50].

2.1. Materials

In the butt welding trial rolled plates of Al alloy 6082-T6 and rolled plates of structural steel S355 were used as base materials (BMs), both having an initial thickness of 4 mm. The other dimensions of the rolled plates were 500 mm × 95 mm. The filler wire (FW) used was of the AA6082-T4 type, produced by HyBond AS. The wire was made from a direct chill cast billet, which then was homogenized, hot extruded and cold drawn down to the final dimension of ∅1.4 mm. The chemical composition of the two BMs and the Al-FW can be found in Table 1 and Table 2, whereas Table 3 contains information about their room temperature mechanical properties.

Note that the FW contains different alloying elements (e.g. Si, Mn, Cr and Zr) that are known to react with other constituent elements and form primary particles and dispersoids during casting, homogenizing and hot extrusion of the blank material used in the wire production [51]. Therefore, it is reasonable to assume that many of the high-temperature phases being present in the FW will survive the passage through the extruder and become trapped in the weld after the joining operation.

2.2. Welding conditions

Prior to welding, surface oxide present on the exposed edges of the steel plate was removed by grinding, whereas the Al plate was used in the as-rolled condition. The two base plates were first mounted in a fixture so that a 3 mm wide I-groove formed between them, as illustrated in Fig. 1(a). Subsequently, the entire welding area was cleaned with acetone to remove remnants of oil and grease inherited from the previous handling of the base plates. During butt welding the extruder head with its ∅7 mm rotating cylindrical pin slides along the joint line at a constant travel speed. At the same time the rotating pin with its moving dies is placed in a submerged position below. Because of the synchronized rotation of the spindle tip and the pin, the FW is continuously dragged into and through the extrusion chamber in the extruder head by friction [36,41]. During the passage through the extrusion chamber the FW loses its structural and mechanical identity due the combination of heating and severe plastic deformation [50]. To emphasise this change of identity the Al is instead termed the FM at the time it hits the stationary abutment intersecting the extrusion chamber. When the required extrusion pressure in front of the abutment is reached, the FM starts to flow downwards in the axial direction and into the groove under high pressure and mix with the Al-BM on the retreating side (RS) of the joint. At the same time, on the advancing side (AS) of the groove, the IMC formation commences as soon as full contact between the FM and the steel wall is reached. Note that having the steel plate located on the AS of the joint means that the down-flow of the FM from the upper part of the extrusion zone (EZ) towards the root region will be most extensive along the Al-steel interface [37]. This creates a vigorous shear flow and optimal conditions for bonding between the FM and the steel during butt welding.

In the present experimental set-up, only the Al groove side wall is supposed to be machined by the pin and not the steel groove wall, as illustrated in Fig. 1(b). Still, the pin may touch the steel because of the lateral oscillations arising from vibrations of the extrusion tool during welding. Table 4 summarizes the operational conditions employed in the HYB butt welding trial. A more in-depth analysis of the essential HYB process parameters and how they are interrelated can be found elsewhere [36].

2.3. Optical microscopy and hardness testing

After the welding operation, cross-sectional samples were extracted from the weld starting area and made ready for metallographic examination using standard preparation techniques. To reveal the weld macrostructure the specimens were first immersed in an alkaline solution of 1 g NaOH per 100 ml H_2O for 3–4 min and then examined in an

Table 1
Chemical compositions (in wt. %) of the AA6082-T6 base material (Al-BM) and the AA6082-T4 filler wire (Al-FW) used in the Al-steel butt welding trial.

Material	Si	Mg	Fe	Cu	Mn	Cr	Zn	Ti	Zr	B	Others	Al
Al-BM	1.21	0.71	0.24	0.060	0.59	0.04	0.04	0.020	–	–	0.150	Balance
Al-FW	1.11	0.61	0.20	0.002	0.51	0.14	–	0.043	0.13	0.006	0.029	Balance

Table 2
Chemical composition (in wt. %) of the S355 steel base material (S-BM) used in the Al-steel butt welding trial.

Material	C	Si	Mn	P	S	Cr	Ni	Cu	Al	Nb	B	N	Fe
S-BM	0.056	0.01	0.46	0.009	0.003	0.02	0.04	0.01	0.041	0.006	0.0001	0.003	Balance

Table 3
Mechanical properties of the aluminium and steel base materials (Al-BM and S-BM) and the cold-drawn AA6082-T4 filler wire (Al-FW) according to mill certificates.

Material	Yield strength [MPa]	Ultimate tensile strength [MPa]	Elongation [%]
Al-BM	325	349	14
S-BM	412	498	28
Al-FW	367	388	4

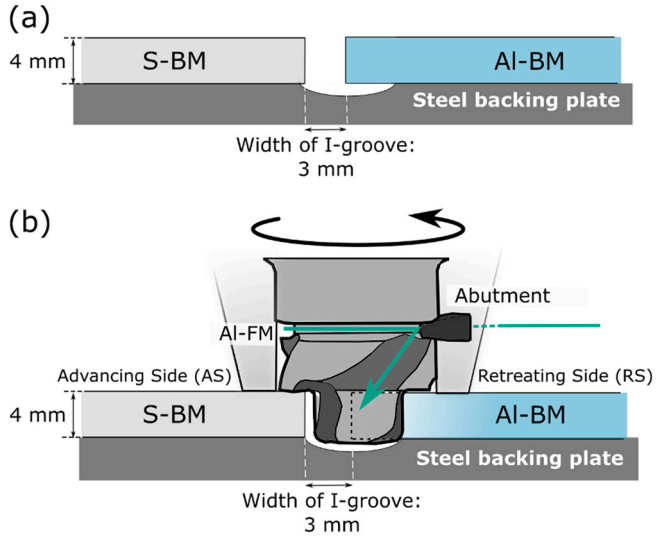

Fig. 1. Schematic illustrations of the experimental set-up during the Al-steel HYB butt welding trial; (a) Transverse cross-section showing the I-groove width and the grooved steel backing plate prior to joining and (b) the pin location within the I-groove during joining. Note that the arrows in the figure indicate the pin rotational direction and the Al-FM flow directions inside the extruder head. The welding direction is out-of-plane.

Table 4
Operational conditions employed in the Al-steel butt welding trial.

Pin rotation [RPM]	Travel speed [mm/s]	Wire feed rate [mm/s]	Gross heat input [kJ/mm]
400	9	155	0.30

Alicona Confocal microscope.

Transverse hardness measurements were made in accordance to ASTM standard E92-16 [52], using a Mitutoyo Micro Vickers hardness testing machine and a constant load of 1 kg. The distance between each indentation was 0.5 mm. The hardness measurements were carried out along the horizontal mid-section of the joint. In total, three individual test series were conducted.

2.4. Scanning and transmission electron microscopy

Flush-machined specimens extracted from the central part of the HYB butt welded plates were used for electron microscopy characterization of the Al-steel interface. SEM examinations were conducted on a mechanically polished cross-section using a dual-beam FEI Helios G4 UX focused ion beam (FIB) microscope and an acceleration voltage of 15 kV. SEM was also employed for fractographic examinations of selected broken tensile specimens. These examinations were carried out using a Quanta FEG 450 SEM and an acceleration voltage of 20 kV.

The Al-steel interface was further characterized using TEM. FIB lift-out was used to fabricate TEM lamellae from the mechanically polished cross-sections. Scanning TEM (STEM) examinations and energy dispersive X-ray spectroscopy (EDS) mapping were performed using a double-aberration corrected JEOL ARM200CF microscope and an acceleration voltage of 200 kV. The EDS maps were analysed using the python library Hyperspy [53], and the analysis included binning, model fitting and quantification by the Cliff-Lorimer method. Moreover, electron diffraction was used to investigate the crystal structure of the IMC layer at the Al-steel interface. Precession electron diffraction (PED) was performed using a JEOL 2100F microscope operated in nano-beam diffraction mode at 200 kV, equipped with a Nanomegas ASTAR system. PED patterns were acquired on an Ultrascan camera, employing a precession angle of 21 mrad and a convergence angle of 1 mrad.

2.5. Tensile testing and DIC analysis

At present, no standard test method exists for tensile testing of dissimilar metal welds. Therefore, sub-size tensile specimens were prepared and tested in accordance with ASTM standard E8/E8M-16a [54], which applies to tensile testing of similar metallic materials. However, to make sure that the entire HAZ on the Al side of the joint was captured by the sampling area, the parallel length of the specimens was extended to 40 mm. In total, two sets of tensile specimens were prepared; one set of reinforced specimens with the weld crowns preserved and one set of flush-machined specimens with slick surfaces. In both cases the specimens have their centres located in the middle of the weld EZ. An overview of the different specimens used for tensile testing is given in Table 5.

Prior to tensile testing the initial cross-sectional area of all specimens was measured. For the reinforced specimens, the measurements were

Table 5
Overview of the different specimens used for tensile testing. Included is also information about their location along the joint line, their labelling and the total number of specimens tested.

Type of specimen	Location along joint line	Labelling	Number of specimens tested
Reinforced specimens with weld crowns preserved	Start, centre, end	TR1, TR2, TR3	3
Flush-machined specimens with slick surfaces	Start, centre, end	TF1, TF2, TF3	3

done adjacent to the weld crowns. Tensile testing was then conducted in a ZwickRoell Z030 electromechanical test machine equipped with a 30 kN load cell, using a cross-head speed of 0.6 mm/min. This corresponds to a nominal strain rate of $2.5{\cdot}10^{-4}$ s^{-1}. In addition, supplementary two-dimensional DIC analysis was carried out to record the strain evolution that occurred in the weld zone during tensile testing. This was done by first painting the transverse cross-section of the specimens with a fine-grained speckled pattern. Then, a high-resolution digital camera was employed to monitor the pertinent changes in the pattern that occurred during deformation. The pictures were taken at a frequency of about 4.8 Hz, employing a resolution of 338 × 2018 and an 8-bit pixel depth. Between 1300 and 1900 images were recorded per test.

The subsequent post-processing of the data was done employing the software developed by Fagerholt et al. [55,56], who utilized a finite element-based technique to solve the intricate correlation problem. In the software a quadratic mesh, having an element size of 25 × 25 pixels, is added onto a reference image of the specimens taken prior to testing, which then is projected onto the stored images taken during loading. From this, the strain evolution within the entire weld zone can be recaptured and presented in the form of two-dimensional field maps. In addition, a virtual extensometer (vector), having a gauge length of 15 mm, was superimposed onto the mesh in order to extract the numerical displacement data needed for the strain analysis.

3. Results

3.1. Transverse hardness profile and weld macrostructure

The results from the transverse hardness measurements along the horizontal mid-section of the HYB joint are presented in Fig. 2 along with a macrograph of the weld cross-section. In this hardness plot each data point represents the average of three individual measurements, while the error bars represent the corresponding standard deviation.

It follows from Fig. 2(a) that the hardness is relatively low within the central region of the joint, being barely higher than 85 HV. Within the EZ there is no significant difference in the hardness between the Al-BM and the FM. On both sides of the EZ the hardness starts to increase. Outside the EZ, on the RS of the joint, the Al-BM hardness of approximately 120 HV is approached after about 2 mm. On the AS, the peak hardness of 243 HV is attained as soon as the indenter hits the steel plate surface. Then, the hardness gradually decreases for about 2 mm until the S-BM hardness of about 180 HV is reached.

Note that the hardness peak on the AS of the joint is believed to be a result of work hardening. One possible explanation is that it is caused by plastic deformation arising from the lateral oscillations of the rotating pin as it travels along the joint line. Also, the extrusion pressure acting in the groove during joining may play a role. This is because adequate bonding in the HYB case implies that the contact pressure must exceed the flow stress of the Al-BM [57]. At present, it cannot be stated with certainty which factor that contributes most to the observed work hardening of the S-BM. Answering that question is beyond the scope of the present investigation and is deferred to a later study.

Fig. 2(b) shows a macrograph of the entire transverse section of the joint, from which the Al-FM and the Al-BM flow patterns can be observed. On the AS of the joint the down-flow of the FM dominates and provides good groove filling, which, in turn, makes bonding between Al and steel possible. Conversely, on the RS of the joint the flow is completely dominated by the rotational action of the pin. In this case the Al-BM is dragged along with the pin and eventually becomes deposited in the groove behind it [36]. In the middle of the EZ, where the two main metal streams meet, some mixing between the Al-FM and the Al-BM occurs.

Fig. 3 shows optical macrographs of the weld root region on the AS of the joint. It follows from Fig. 3(a) that small steel fragments are present inside the Al-FM a short distance (about 0.4–0.7 mm) from the Al-steel interface. This provides further evidence of direct contact between the pin and the S-BM during welding. Also, small defects can be observed inside the root crown. As shown in Fig. 3(b), one of these arises from incomplete bonding between the two parallel metal streams. However, because the defect is of the internal type and at the same time parallel to the base plate surface, it is not expected to be devastating for the tensile properties. The same is also true for the other one located inside the root crown, which appears to be a surface defect arising from some incidental rubbing contact between the Al-BM and the steel backing plate.

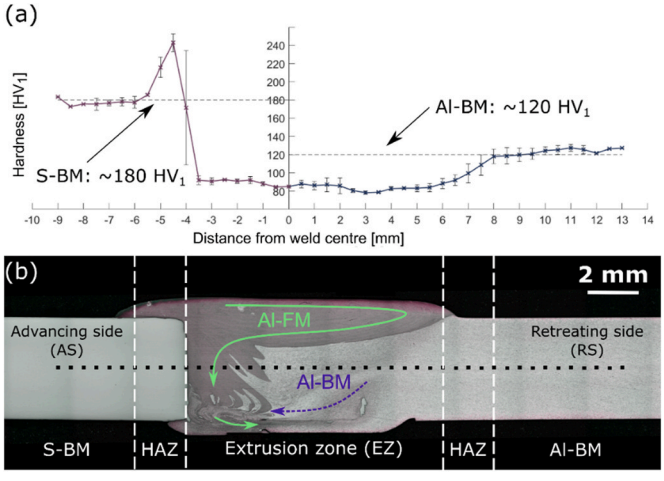

Fig. 2. (a) Measured transverse hardness profile and (b) optical macrograph of the 4 mm thick Al-steel HYB butt weld. The horizontal dashed lines in (a) represent the Al-BM and the S-BM hardness, respectively, whereas the horizontal dotted line in (b) indicates the location of the hardness impressions. Note that in the hardness profile each data point is the average of three individual measurements, while the error bars represent the corresponding standard deviation.

3.2. SEM examination of the Al-steel interface

The HYB weld was further examined in SEM to reveal the underlying bonding mechanisms. Fig. 4 shows backscatter electron (BSE) images of the Al-steel interface. From the overview image in Fig. 4(a) it appears that the interface becomes increasingly wavy towards the weld root region. Moving on to the close-up of the weld root region in Fig. 4(b), it is evident that steel fragments of various sizes are embedded in the Al-FM. At a higher magnification, the coarse nature of the interface becomes apparent, as shown by the BSE image in Fig. 4(c). Also, the IMC layer enclosing the Al-steel interface is visible. In this particular image the IMC layer thickness is seen to vary between 0.4 and 0.9 μm, whereas at other locations along the interface it is smaller (i.e. closer to 0.1 μm). Still, the observed thickness is significantly larger than that reported for the IMC layer in the second generation Al-steel HYB butt weld, which typically is between 10 and 50 nm in the midsection of the joint [42].

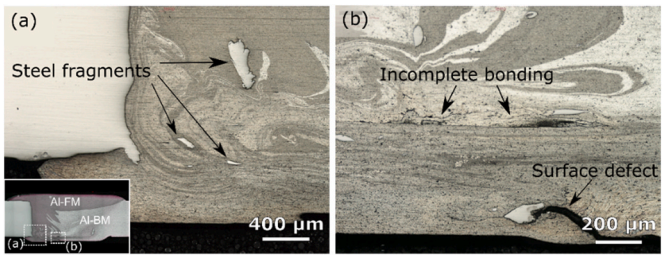

Fig. 3. Optical macrographs of the weld root region on the advancing side of the joint; (a) Small steel fragments observed inside the Al-FM a short distance away from the Al-steel interface and (b) defects detected inside the weld root crown.

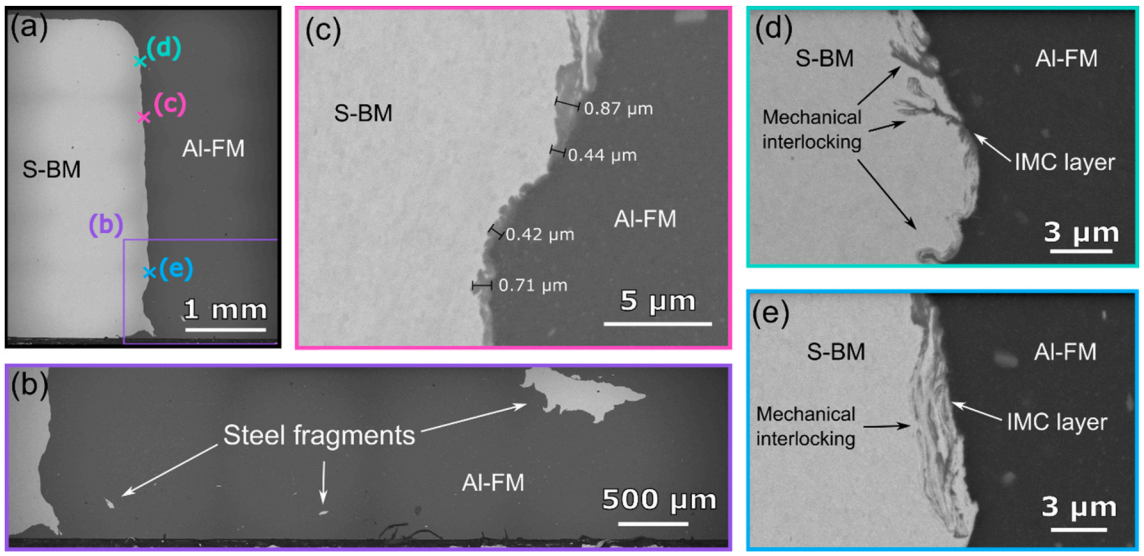

Fig. 4. SEM BSE images highlighting different features of the Al-steel interface in the HYB butt weld; (a) Overview image of the microscopic wavy nature of the Al-steel interface, (b) low magnification image revealing the embedded steel fragments located inside the root region of the Al-FM, (c) high magnification image showing the coarse appearance of the interface and the IMC layer enclosing it, (d) and (e) shows high magnification images revealing irregular details of the interface close to the weld face and root region, respectively.

Finally, evidence of mechanical interlocking between Al and steel at the interface is provided by the SEM BSE images in Fig. 4(d) and (e). It follows that the HYB Al-steel interface at a high magnification is irregular and bears a close resemblance to the Al-steel interface recently reported for a corresponding lap joint produced using the so-called Friction Stir Scribe Welding (FSSW) process [58]. In FSSW it is a premise that mechanical interlocking and IMC formation occur simultaneously during the welding operation to ensure a highest possible bond strength [58,59]. The same two bonding mechanisms are also observed in the present Al-steel HYB butt weld.

3.3. TEM examination of the Al-steel interface

TEM examination of the Al-steel interface was carried out to provide information about the morphology, chemical composition and crystal structure of the IMC layer. Fig. 5(a) shows a bright field (BF)-TEM image of the interface in the lower region of the HYB joint. Again, the irregular appearance of the interface is visible. Still, the IMC layer is continuous across the entire TEM lamella with an average thickness of 0.22 μm. Also intermixed regions of Al-FM and S-BM can be detected, as indicated in Fig. 5(a). From this BF-TEM image it can be seen that the morphology of the IMC layer varies along the Al-steel interface. In some regions the layer appears dense, while other regions contain IMC grains partly separated by regions of Al-FM. This can also be seen in the high angle annular dark field (HAADF)-STEM image in Fig. 5(b). Fig. 5(c) shows element maps based on STEM EDS, providing information about the relative content of the major constituent elements (in at.%). It follows that the IMC layer is mainly composed of one Al–Fe–Si phase containing small amounts of Mn. In addition, adjacent to the IMC layer a single Mg–Si particle along with some Al–Mn–Cr–Si-containing dispersoids and a few trapped oxide particles are observed within the Al-FM. These phases (perhaps with the exception of the oxides) are mainly believed to be exogeneous in the sense that they form by precipitation reactions occurring at high temperatures during casting, homogenizing and hot

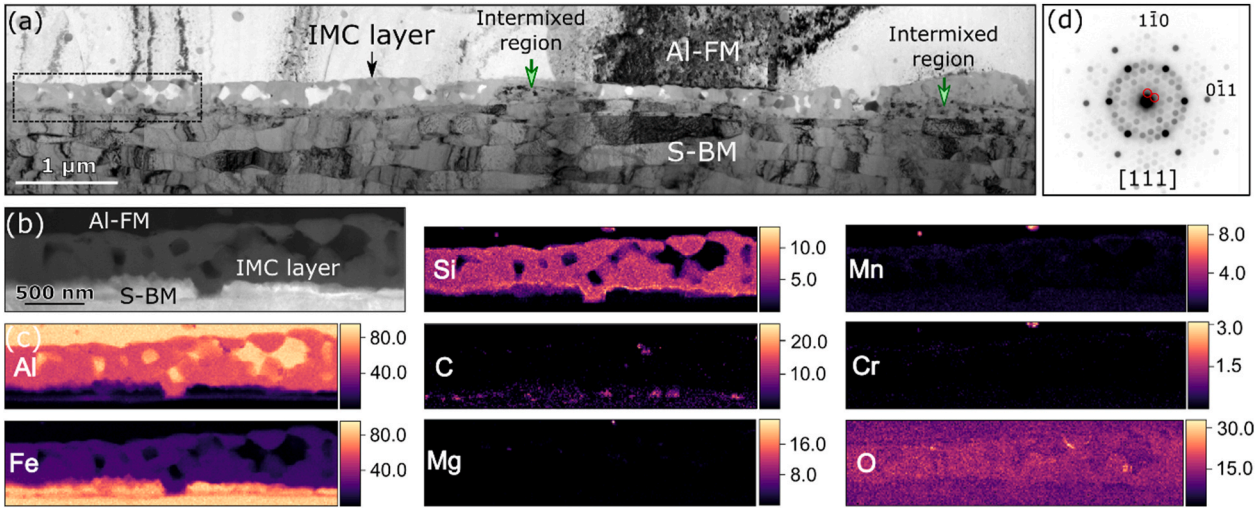

Fig. 5. TEM characterization of the HYB Al-steel interface; (a) BF-TEM image of the interface region, (b) enlarged HAADF-STEM image of the dashed rectangle outlined in (a), (c) element maps based on STEM EDS of the interface region, where the relative composition is shown in at.%, (d) indexed PED pattern for an IMC crystal oriented along the [111] zone axis conforming to the cubic α_c-Al-(Fe,Mn)–Si phase.

extrusion of the blank material used in the Al-FW production [51]. Hence, they are brought into the system by the Al-FM, as opposed to the IMC reaction layer, which forms at the Al-steel interface during the extrusion & joining process.

Since there are several possible candidate Al–Fe–Si phases [60,61], electron diffraction was employed to determine which phase(s) the IMC layer consisted of. Fig. 5(d) shows a PED pattern obtained from one of the grains in the IMC layer oriented along the [111] zone axis. The subsequent indexing of the PED patterns fits the cubic α_c-Al-(Fe,Mn)–Si phase ($Im\bar{3}$, #204, $a = 12.6$ Å) [62]. This α_c-phase generally forms in Al alloys containing Si, Fe and Mn, and the IMC phase detection therefore agrees with the Al-FM composition data in Table 1. The α_c-phase has also been reported in studies of comparable Al-steel joints, including the second generation Al-steel HYB weld [11,15,42,63,64].

3.4. Tensile test results

In Al welds the measured values of the yield strength and fracture strain depend on the position of the extensometer within the weld zone [39]. Therefore, to obtain reliable data for these two quantities in the present Al-steel HYB joint, it is important that all major deformation zones are properly sampled by the extensometer.

As a starting point, two-dimensional DIC field maps are used to visualize the evolution of the plastic deformation fields inside the specimens during tensile testing. Fig. 6 shows snap-shots taken immediately before final fracture occurs in two representative specimens. In both cases most of the plastic deformation is localized to the soft HAZ on the Al side of the joint. In contrast, the S-BM appears to be essentially unaffected by the applied tensile load. Hence, to ensure reliable readings the virtual extensometer must be placed outside the steel part and within the central parts of the EZ and the HAZ on the Al side of the joint, as shown in Fig. 6.

The main results from the tensile testing, using the location of the virtual extensometer in Fig. 6, are presented in Fig. 7 along with corresponding data for the Al-BM (from Table 3). It follows from Fig. 7 that the reinforced tensile specimens (with both weld crowns preserved) generally display higher strength values compared to the flush-machined tensile specimens. This means that the reinforcement provides an additional strength increase under the prevailing circumstances. Still, the measured yield and tensile strength values are significantly lower than those of the Al-BM, reflecting the fact that also the present Al-steel HYB butt weld suffers from severe HAZ softening on the Al side of the joint. Moreover, Fig. 7 displays the results from the fracture strain measurements for the same sets of tensile specimens. In general, the flush-machined specimens exhibit the highest fracture strain values (i.e. 11 % *vs*. 7% for the reinforced specimens). However, both types of weld samples display a lower tensile ductility compared to the Al-BM. This is because they have been exposed to considerable strain localization and necking in the HAZ prior to fracture, whereas the Al-BM undergoes a more uniform deformation behaviour.

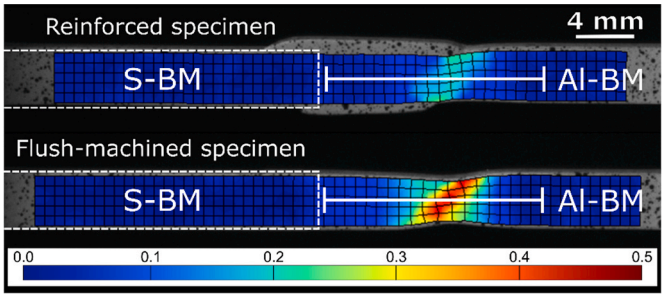

Fig. 6. Two-dimensional DIC field maps showing snap-shots of the effective principal strain evolution within two selected tensile specimens (i.e. TR2 and TF2) immediately before final fracture occurs. Note that the white, solid scale bars in the figure indicate the approximate location of the virtual extensometer used in the strain measurements, whereas the white, broken rectangles indicate the outer contour of the S-BM.

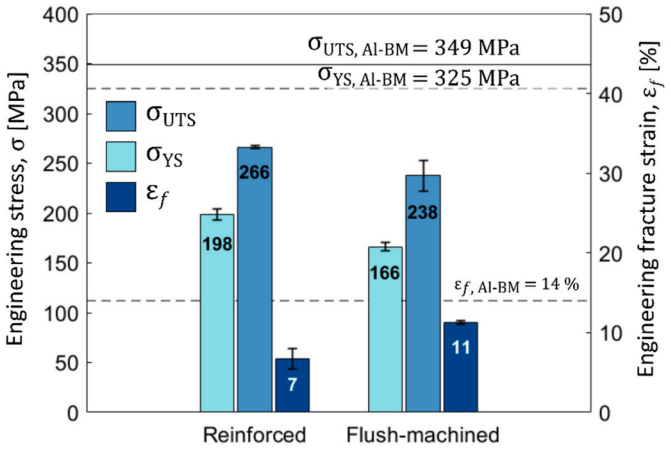

Fig. 7. Results from tensile testing of the Al-steel HYB butt weld using two different types of tensile specimens, showing their offset yield strengths (σ_{YS}), ultimate tensile strengths (σ_{UTS}) and fracture strains (ε_f). Note that the values indicated by the solid bars in the graph represent the average of three individual measurements, while the error bars represent the corresponding standard deviation.

3.5. Fracture analyses

Following tensile testing, the broken specimens were visually examined and photographed, as shown in Fig. 8. As can be seen from these photographs, final fracture always occurs in the soft part of the HAZ on the Al side of the joint, regardless of the specimen geometry. This is even true for the TR3 and TF3 specimens, which contain large visible voids prior to tensile testing because of some temporary instability in the Al-FW feeding during extrusion & joining. Hence, in the present Al-steel butt weld the bonded interface is not the weakest part of the joint. This behaviour is in sharp contrast to that experienced during tensile testing of the second generation Al-steel HYB butt weld, where interfacial cracking is seen to be the dominating failure mechanism [42].

The observed change to a more favourable failure mode does not mean that the present Al-steel HYB butt weld is free from flaws. For example, the flush-machined TF3 tensile specimen, which revealed the lowest UTS (i.e. 220 MPa), suffers both from void formation and lack of bonding in the root region, as shown by the SEM fractographs in Fig. 9. However, as long as the flaws are located inside the EZ, they do not trigger crack propagation along the bonded interface but leads to ductile fracture in the Al through dimple formation. As a matter of fact, this failure mode is observed in all tensile specimens tested, irrespectively of whether they contain flaws or not.

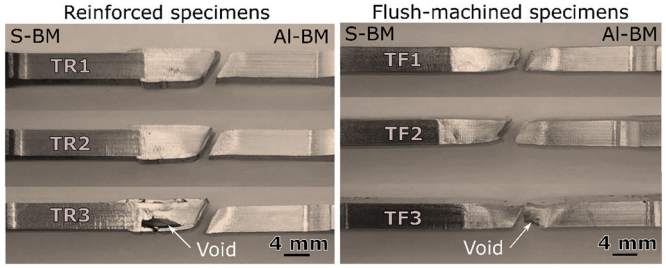

Fig. 8. Photographs showing the location of the final fracture in the broken tensile specimens. Note that two of the specimens (TR3 and TF3) contained large visible voids prior to testing.

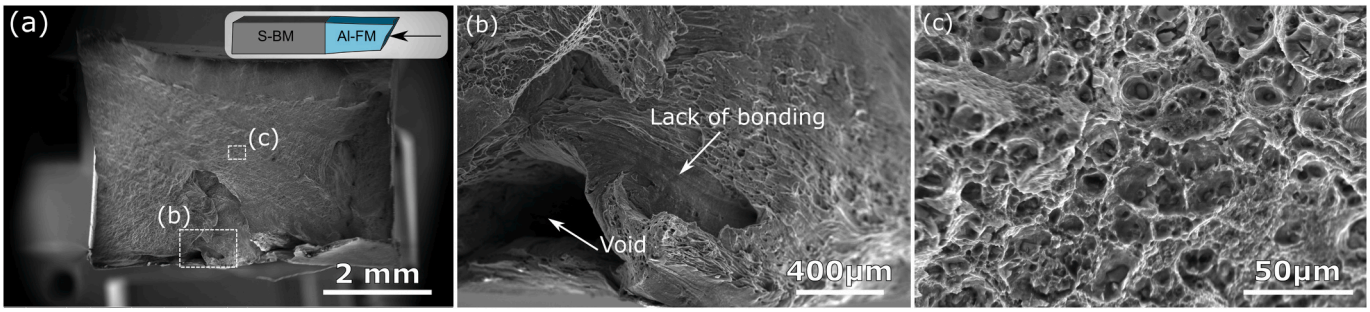

Fig. 9. SEM fractographs of the broken tensile specimen TF3; (a) Low-magnification image revealing its entire fracture surface, (b) close-up showing evidence of void formation and lack of bonding within the root region and (c) close-up revealing evidence of extensive dimple formation within the central part of the fracture surface.

4. Discussion

4.1. Factors affecting the Al-steel interface microstructure and resulting bond strength

In the absence of other defects, the strength of Al-steel welds is governed by the interface characteristics and mainly the IMC layer thickness [5,12–14,49,65–67]. Although a thin IMC layer is normally considered to promote a high bond strength, the reported critical thickness range where interfacial cracking occurs is relatively large (i.e. varies from about 50 nm to 5 µm) [5,12,14,47,68]. Therefore, the bond strength is also influenced by a number of other factors. For instance, in solid state joining of Al to steel, where the interface microstructure is complex, both the IMC layer continuity [5,69], its chemical composition [13,70] and morphology [47,49,71] will affect the resulting weld tensile properties. The formation and extent of these microstructural features depend, in turn, on the applied welding conditions, i.e. the chosen processing parameters, the tool design and in the HYB case also the position of the rotating pin inside the weld groove [4,67,70,72]. Hence, to better understand the shift in the fracture behaviour between the second and the third generation Al-steel HYB welds additional factors related to the pertinent differences in the experimental conditions need to be taken into consideration to elucidate why the latter weld displays the most crack resistant interfacial microstructure and thus the highest bond strength of the two.

Fig. 10 shows simplified schematic drawings of the experimental set-up and interface microstructure of the second and third generation Al-steel HYB butt welds. These drawings are included to highlight the pertinent differences in the resulting IMC layer thickness and the interface morphology between the two welds, which are produced under otherwise similar welding conditions. A detailed report on the mechanical and microstructural characterization of the second generation Al-steel HYB weld can be found in the work by Bergh *et al.* [42].

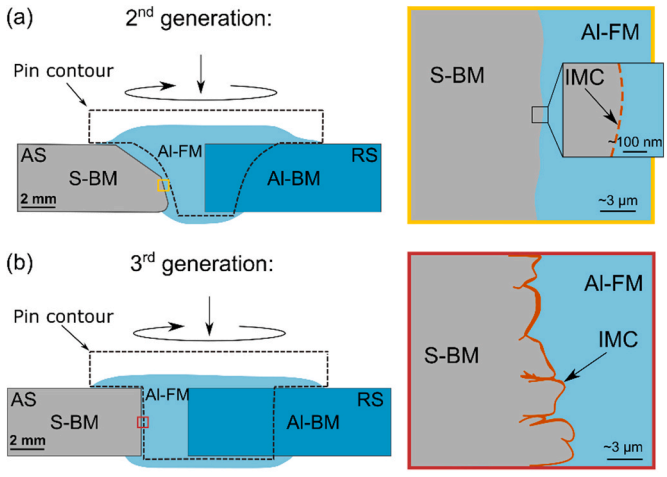

Fig. 10. Schematic drawings of the weld configuration, pin location and the resulting Al-steel interface microstructures in two different Al-steel HYB butt welds; (a) Second generation and (b) third generation.

From Fig. 10(a) and (b), it can be seen that the main difference between the second and third generation Al-steel HYB welds is the positioning of the rotating pin within the weld groove, which in the latter case enables direct physical contact with the steel during the joining operation leading to a coarse and wavy Al-steel interface. At the same time, the experimental set-up used in the fabrication of the third generation HYB weld leads to a more vigorous material flow along the entire Al-steel interface. Both factors favour bonding by a combination of mechanical interlocking and IMC formation, as illustrated in Fig. 10(b). In contrast, the IMC layer in the second generation Al-steel butt weld is much thinner (i.e. between 10 and 50 nm) and discontinuous, as indicated by the sketch in Fig. 10(a).

In order to explain the pertinent difference in the IMC layer thickness between the second and the third generation Al-steel HYB welds, one needs to focus on possible factors influencing the growth kinetics. Both the second and the third generation Al-steel HYB welds were produced using rolled plates of Al alloy 6082-T6 and structural steel S355. The elements in the steel BM known to influence the IMC layer growth are Si, Mn, Cu and Ni [9,10], but a comparison between the two steel BMs shows only minor differences in the content of these elements. Also the Al-FW used in the two Al-steel HYB butt welds are identical. Hence, the effect of variations in the BM and the FM chemical compositions is deemed to be insignificant and should therefore not affect the IMC growth kinetics in the present case.

On the other hand, the observed difference in the IMC layer thickness between the second and the third generation of Al-steel HYB butt welds can be understood if one starts to realize how the steel-pin interaction affects the interface temperature. Unfortunately, no *in-situ* thermocouple measurements are available for a direct comparison of the weld thermal programmes, but a likely scenario is presented in Fig. 11(a). This is based on a qualitative judgement of the way the peak temperature of the thermal cycles at the Al-steel interface becomes shifted upwards by the additional heat being generated when the pin hits the steel groove wall. The next step in the analysis is to invoke the isokinetic diffusion model developed previously by the same authors for the IMC formation in Al-steel welds [16]. Based on this model it can be rationalized that an increase in the peak temperature, from, say, 300–350 to 500-550 °C, is more than sufficient to increase the IMC layer thickness from 0.01 to 0.05 µm and up to 1 µm, as illustrated in Fig. 11(b). An IMC layer thickness of about 1 µm is also typical of friction stir-welded Al-steel joints [5,16], where the tungsten carbide (WC) tool pin is forced to machine the steel plate during the joining operation.

Finally, the cracking resistance of the different HYB Al-steel interface microstructures will be briefly commented on. If one just considers the isolated effect of the IMC layer thickness, the thin nanolayer observed in the second generation Al-steel HYB butt weld would be expected to exhibit the highest bond strength as long as it is continuous, considering

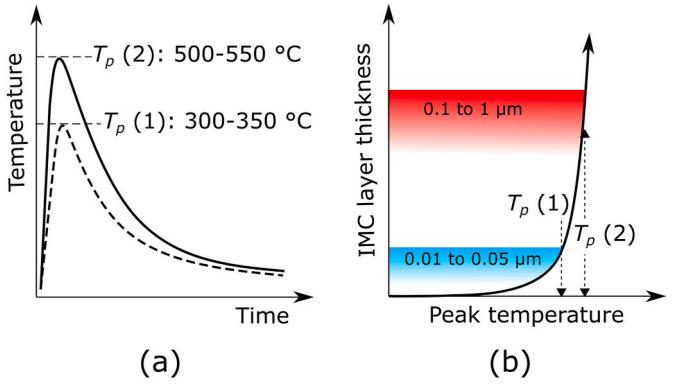

Fig. 11. Schematic drawings showing how the interface temperature and microstructure become affected by the additional heat being generated when the pin hits the steel groove wall; (a) Shift in the peak temperature of the thermal cycles from T_p (1) to T_p (2), (b) resulting effect of this temperature increase on the subsequent growth of the IMC layer.

the fact that the layer is composed of nanocrystals acting as effective barriers against crack propagation [16]. Still, the weld is vulnerable to interfacial cracking during tensile loading, as it suffers from lack of bonding in the root region. Although the observed IMC layer is thicker in the third generation Al-steel HYB butt weld, it is deemed to exhibit a more favourable interface microstructure from a cracking resistance point of view. This is because the IMC layer appears continuous along the entire Al-steel joint line and displays a bond strength that is sufficiently high to promote failure by necking in the soft HAZ on the Al side of the joint. In addition, the microscale mechanical interlocking maximizes the interfacial contact area and inhibits interfacial cracking of the IMC layer because of its shifting directionality. At the same time, the Al-steel interface is firmly held together by the inclosing IMC layer, which in this case acts as an adhesive. The advantages of mechanical interlocking is also observed by others [73,74]. As a matter of fact, in Al-steel welds produced using the FSSW process this interface microstructure is the targeted one, since it is known to provide the highest bond strength [58]. Therefore, its formation should also be promoted in the HYB case in the future.

4.2. The tendency to shear fracture on the aluminium side of the joint during tensile loading

It follows from the photographs previously presented in Fig. 8 that both types of tensile specimens reveal evidence of shear fracture on the Al side of the joint. A comparison with the DIC field maps in Fig. 6 shows that the shear fracture is a result of the strain localization occurring within the soft part of the HAZ during testing. In AA6082-T6 weldments, the soft zone typically falls within the 300–400 °C HAZ isotherms, which in the present Al-steel HYB butt weld approximately coincide with the direction for the maximum shear stress τ_{max} in the tensile specimens. This can easily be verified through an evaluation of the thermal field and the shape of the same HAZ isotherms during single pass butt welding of 4 mm thick plates at comparable heat inputs [75].

The stress state existing during tensile testing is further elaborated in Fig. 12(a). To simplify the problem we first invoke the Tresca yield criterion [76], which makes it possible to correlate τ_{max} directly to the local yield stress in tension σ_0 inside the soft HAZ. Hence, we may write $\tau_{max} = \sigma/2 = \sigma_0/2$. Based on this relationship the stress-load response diagram in Fig. 12(b) has been constructed for the specific tensile specimen geometry used in the present investigation.

It follows from Fig. 12(b) that the flush-machined tensile specimens will start to yield as soon as the maximum shear stress τ_{max} reaches the local yield shear strength $\tau_0 = 83$ MPa inside the soft HAZ. This corresponds to a tensile yield strength of 166 MPa, as shown previously by the

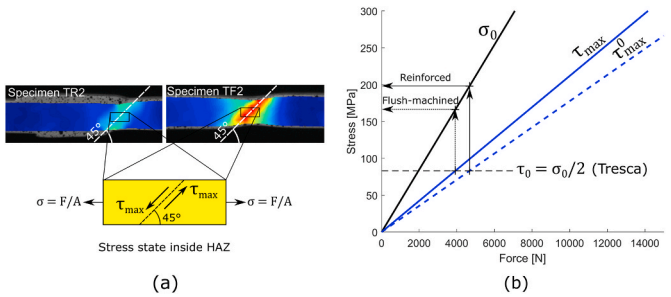

Fig. 12. Evaluation of the conditions leading to shear fracture on the aluminium side of the Al-steel HYB butt weld during tensile testing; (a) Location of the maximum shear stress inside the tensile specimens, (b) mechanical response of the flush-machined and fully reinforced tensile specimens to the applied tensile loading.

data presented in Fig. 7. In the case of the fully reinforced specimens, the increased cross-sectional area provided by the outmost part of the root crown must also be taken into consideration. This part falls inside the soft part of the HAZ and will be in-line with the 45° direction for the maximum shear stress (see Fig. 12(a)). Because of the thickness increase, a higher force F needs to be applied during testing of the fully reinforced tensile specimens before the maximum shear stress τ^0_{max} reaches the same local yield shear strength of 83 MPa inside the soft HAZ. This extra force is registered as an increase in the yield tensile strength, as shown in Fig. 12(b). The same type of argument can also be used to explain the higher UTS values being observed for the fully reinforced tensile specimens in Fig. 7. Hence, the root crown of the present Al-steel HYB butt weld is seen to play a role in the mechanical testing by reducing the significance of the strength loss within the soft HAZ on the Al side of the joint.

4.3. Benchmarking of the HYB method against other welding processes

Finally, it is worthwhile to compare the tensile properties of the Al-steel HYB butt welds with those reported in the literatures for similar types of welds produced using commercial methods like gas tungsten arc welding (GTAW), pulsed GMAW (PGMAW) and conventional GMAW, laser beam welding (LBW), CMTW and FSW along with different combinations of these processes (so-called hybrid variants). Table 6 contains a compilation of the data for the different Al-steel butt welds being used in the benchmarking of the HYB process, covering a wide range of methods, material combinations, plate thicknesses and Al-BM strength levels.

To obtain a fair and meaningful comparison, two different graphs have been constructed. The first one is presented in Fig. 13(a), which shows plots of UTS weld vs. UTS Al-BM for selected combinations of welding process and BMs. The two straight lines in the diagram highlights the spread in the reported joint efficiencies. As expected, Al-steel welds produced using fusion welding processes like LBW, GMAW, GTAW, CMTW or different hybrid variants generally yield the lowest joint efficiencies, whereas the FS welds display the highest ones. The joint efficiency of the Al-steel HYB welds is seen to fall in-between the 100% and the 50% limits. Obviously, these process-related differences in the joint efficiency can be attributed to variations in the interface microstructure and, in particular, the thickness of the IMC layer, which during fusion welding is typically between 2 and 20 μm. A thick IMC layer increases the risk of interfacial cracking during tensile loading. However, if the comparison instead is based on the absolute UTS values, the present Al-steel HYB butt weld comes out second best, only beaten by the hybrid (FSW + GTAW) weld, as shown in Fig. 13(a).

Alternatively, the same UTS weld values can be plotted as a function of the applied welding speed. This plot is shown in Fig. 13(b). Although the spread in the data is admittedly large, it is still possible to extract

Table 6
Summary of literature data for different Al-steel butt welds used in the benchmarking of the HYB process. Included is information on the applied welding methods, base metal (BM) combinations, welding speeds, and the ultimate tensile strength (UTS) levels of both the Al-BM and the weldments.

Type of process	Welding method(s)	Material combinations		Welding speed [mm/s]	σ_{UTS} values [MPa]		Source
		Al-BM	S-BM		Al-BM	Weld	
Fusion welding	PGMAW	AA5052/1.5 mm	Galvanized/1.2 mm	10	200	120	[77]
	LBW	AA6061-T6/1.5 mm	DP590/1.2 mm	8.3	310	208	[78]
	LBW	AA6061-T6/2 mm	DP590/2 mm	8.3	310	142	[79]
	LBW	AA6061/1.15 mm	H220YD/1.2 mm	16.7	230	162	[80]
	LBW	AA6061-T6/2.1 mm	AISI304/1.8 mm	33.3	290[a]	160	[81]
	LBW	AA6061-T6/2 mm	DP590/2 mm	8.3	310	141	[82]
Hybrids	LBW + GMAW	AA6061-T6/2 mm	STS304/2 mm	8	290	200	[83]
	LBW + GMAW	AA6016-T4/1.15 mm	DC05+ZE/1 mm	100	250[a]	200	[31]
	LBW + CMTW	AA5052/2 mm	Q235/2 mm	33.3	170	83	[84]
	LBW + CMTW	AA6A01-T5/2.5 mm	SUS301L/2 mm	20	245	189	[18]
	FSW + LBW	AA6061-T6/3 mm	Q235/3 mm	0.4	270	196	[32]
	FSW + GTAW	AA6061-T6/3 mm	STS304/3 mm	0.8	310	290	[46]
Solid state	FSW	AA5083/2 mm	SS400/2 mm	0.42	275	237	[43]
	FSW	AA5052-H32/3 mm	HSLA/3 mm	0.75	209	196	[5]
	FSW	AA5083-H321/5 mm	STS316L/5 mm	2.7	320	238	[44]
	FSW	AA6061-T6/1.5 mm	TRIP780/1.4 mm	1.5	283	240	[49]
	FSW	AA6061-T6/6 mm	SS400/6 mm	1.2	315	240	[20]
	FSW	AA6061-T6/6 mm	AISI108/6 mm	2.3	303	117	[19]
	FSW	AA6061-T6/3 mm	STS304/3 mm	0.5	405	255	[45]
	FSW	AA6061-T6/3 mm	STS304/3 mm	0.8	310	250	[46]
	FSW	AA6181-T4/1.5 mm	HC260LA/1.5 mm	8	259	200	[47]
	FSW	AA6181-T4/1.5 mm	DP600/1.5 mm	8	259	211	[47]
	FSW	AA6063-T5/5 mm	S45C/5 mm	16.7	212	160	[85]
	FSW	AA6061-T6/1.5 mm	TRIP780/800/1.5 mm	2	283	252	[48]
	FSW	AA6061-T6/1.5 mm	TRIP780/800/1.5 mm	1	283	249	[48]
	HYB-2.gen.	AA6082-T6/4 mm	S355/4 mm	6	306	221	[42]

[a] From standard NS-EN 485–2:2016+A1:2018.

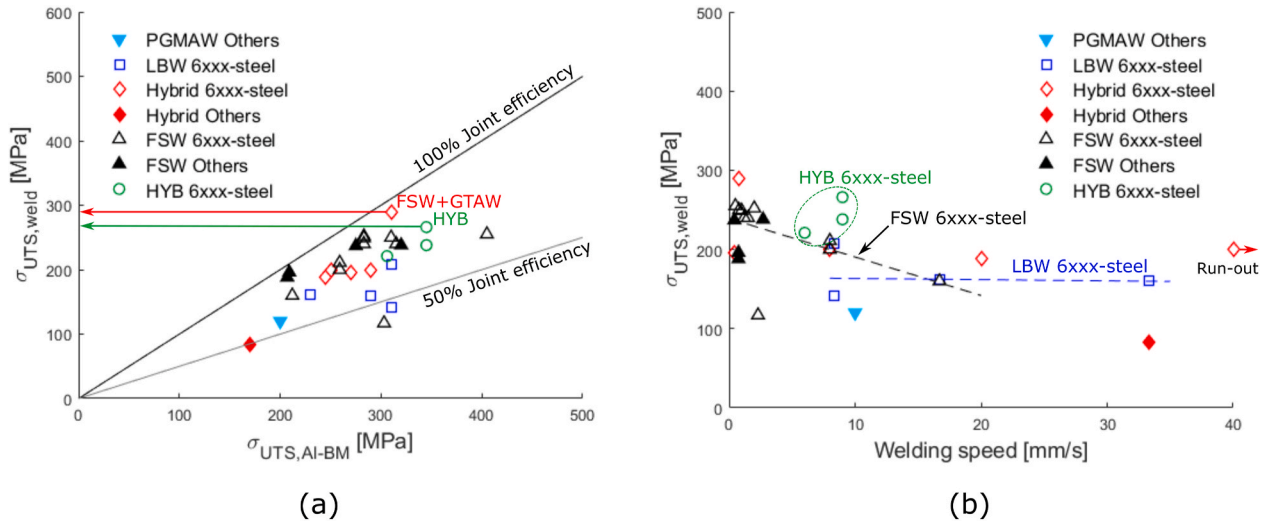

Fig. 13. Benchmarking of the HYB process against other methods used for butt welding of Al to steel; (a) Plots of UTS weld *vs.* UTS Al-BM for selected combinations of process and base materials, (b) plots of UTS weld *vs.* welding speed for the same combinations of process and base materials. Input data from Table 6.

some interesting trends from the graph by focusing on specific combinations of welding process and BMs. It follows from the trendline representing LBW of 6xxx Al alloys to steel that this process allows welding at high speeds. However, the tensile properties achieved are modest and appear to be independent of the applied welding speed. In the FSW case the situation is opposite. As shown by the FSW 6xxx-steel trendline in Fig. 13(b), the highest UTS weld values are obtained when the welding speed is low. This has to do with the fact that during FSW the steel plate must be machined by the WC tool pin to ensure a high bond strength, which, in turn, requires the use of a low welding speed. In the HYB case, matching UTS strength levels can be achieved at much higher welding speeds because there is no need for the tool pin to machine the steel. Apparently, it is sufficient that the tool pin just touches the steel groove wall during the joining operation to create a strong bond through the combination of mechanical interlocking and IMC formation, as indicated by the encircled tensile test data representing the HYB welds in Fig. 13(b).

5. Conclusions

The main conclusions that can be drawn from this investigation are as follows:

- The third generation Al-steel HYB butt welds exhibit excellent tensile properties, displaying ultimate tensile strength (UTS) values in the range from 238 to 266 MPa. In these welds fracture occurs by

necking in the soft heat-affected zone (HAZ) on the aluminium (Al) side of the joint.

- Digital image correlation analysis reveals that all plastic deformation in the Al-steel HYB weld is localized to the soft HAZ on the Al side of the joint. In contrast, the steel base metal appears to be essentially unaffected by the applied tensile load. Hence, to ensure reliable readings for the yield strength (YS) and the fracture strain, it is important that the virtual extensometer is placed outside the steel and within the central parts of the extrusion zone and the HAZ on the Al side of the joint.
- Because the contour of the soft HAZ in the Al-steel HYB butt weld approximately coincides with the 45° direction for the maximum shear stress in the specimens, both the fully reinforced tensile specimens and the flush-machined tensile specimens fail by shear fracture in that zone. Still, the fully reinforced specimens show higher YS and UTS values. This reflects the fact that the weld root crown also plays a role in the mechanical testing by reducing the significance of the strength loss within the soft HAZ on the Al side of the joint.
- The SEM and TEM examinations of the Al-steel interface show that bonding in the HYB weld occurs by a combination of microscale mechanical interlocking and intermetallic compound (IMC) formation. The IMC layer appears continuous along the joint line and the thickness typically varies from 0.1 to 1 μm. The IMC layer is composed of cubic crystals of the α_c-Al-(Fe,Mn)–Si type. Thus, the resulting bond strength is attributed to the combination of microscale mechanical interlocking and the irregular morphology of the nanoscale Al–Fe–Si layer. Both factors contribute to minimize the risk of interfacial cracking during tensile loading.
- Benchmarking of the HYB process against other commercial methods currently being used for Al-steel butt welding has been conducted, based on a comparison of data reported for the weld UTS. The commercial methods in question are gas tungsten arc welding, pulsed and conventional gas metal arc welding, laser beam welding, cold metal transfer welding and friction stir welding (FSW) along with different combinations of these processes. The benchmarking shows that the tensile properties of the present Al-steel HYB butt weld surpass those reported for comparable FS welds, which yield the highest UTS values of all commercial methods. At the same time, the HYB process allows butt welding to be performed at much higher speeds compared to FSW, without compromising the mechanical integrity of the weldment.
- Further optimization of the HYB process is needed in order to reach its full potential for Al-steel welding. Still, in its current developed stage, the mechanical integrity of the third generation Al-steel HYB welds is sufficiently high to justify further examinations of the joint, including high-cycle axial fatigue testing. This work is now in progress.

CRediT authorship contribution statement

Lise Sandnes: Conceptualization, Writing – original draft, Project administration, Visualization, Investigation, mechanical characterization, Formal analysis, related to mechanical testing. **Tina Bergh:** Investigation, SEM/TEM, Analysis – SEM/TEM characterization, Formal analysis, related to SEM/TEM characterisation. **Øystein Grong:** Resources, Writing – review & editing, Supervision, Validation, overall work. **Randi Holmestad:** Validation, SEM/TEM, Supervision. **Per Erik Vullum:** Validation, SEM/TEM, Supervision. **Filippo Berto:** Validation, mechanical testing and fractography, Supervision.

Declaration of competing interest

The authors declare that they have no known competing financial interests or personal relationships that could have appeared to influence the work reported in this paper.

Acknowledgements

The authors acknowledge the financial support from HyBond AS, NTNU and NAPIC (NTNU Aluminium Product Innovation Center), together with the financial support from the Research Council of Norway through SFI Manufacturing (project number 237900), NORTEM (project number 197405) and NorFab (project number 245963/F50). They are also indebted to Ulf Roar Aakenes and Tor Austigard of HyBond AS for valuable assistance in producing the Al-steel HYB butt weld examined in the present investigation.

References

[1] M.M. Atabaki, M. Nikodinovski, P. Chenier, J. Ma, M. Harooni, R. Kovacevic, Welding of aluminum alloys to steels: an overview, J. Manuf. Sci. Prod. 14 (2) (2014) 59–78, https://doi.org/10.1515/jmsp-2014-0007.
[2] L. Wan, Y. Huang, Friction stir welding of dissimilar aluminum alloys and steels: a review, Int. J. Adv. Manuf. 99 (5–8) (2018) 1781–1811, https://doi.org/10.1007/s00170-018-2601-x.
[3] W. Cai, G. Daehn, A. Vivek, J. Li, H. Khan, R.S. Mishra, M. Komarasamy, A state-of-the-art review on solid-state metal joining, J. Manuf. Sci. Eng. 141 (3) (2019), https://doi.org/10.1115/1.4041182.
[4] S.A. Hussein, A.S.M. Tahir, A.B. Hadzley, Characteristics of aluminum-to-steel joint made by friction stir welding: a review, Mater. Today Commun. 5 (2015) 32–49, https://doi.org/10.1016/j.mtcomm.2015.09.004.
[5] K.K. Ramachandran, N. Murugan, S. Kumar, Friction Stir Welding of Aluminum Alloy AA5052 and HSLA Steel: mechanical and microstructural characterization of dissimilar friction stir welded butt joints, Weld. J. 94 (2015) 291–300.
[6] V. Jindal, V. Srivastava, Growth of intermetallic layer at roll bonded IF-steel/aluminum interface, J. Mater. Process. Technol. 195 (1–3) (2008) 88–93, https://doi.org/10.1016/j.jmatprotec.2007.04.118.
[7] V. Jindal, V.C. Srivastava, A. Das, R.N. Ghosh, Reactive diffusion in the roll bonded iron–aluminum system, Mater. Lett. 60 (13) (2006) 1758–1761, https://doi.org/10.1016/j.matlet.2005.12.013.
[8] L. Xu, J.D. Robson, L. Wang, P.B. Prangnell, The influence of grain structure on intermetallic compound layer growth rates in Fe-Al dissimilar welds, Metall. Mater. Trans. 49 (2) (2018) 515–526, https://doi.org/10.1007/s11661-017-4352-y.
[9] W.-J. Cheng, C.-J. Wang, Effect of silicon on the formation of intermetallic phases in aluminide coating on mild steel, Intermet 19 (10) (2011) 1455–1460, https://doi.org/10.1016/j.intermet.2011.05.013.
[10] B. Dangi, T.W. Brown, K.N. Kulkarni, Effect of silicon, manganese and nickel present in iron on the intermetallic growth at iron - aluminum alloy interface, J. Alloys Compd. 769 (2018) 777–787, https://doi.org/10.1016/j.jallcom.2018.07.364.
[11] L.A. Jácome, S. Weber, A. Leitner, E. Arenholz, J. Bruckner, H. Hackl, A.R. Pyzalla, Influence of filler composition on the microstructure and mechanical properties of steel—aluminum joints produced by metal arc joining, Adv. Eng. Mater. 11 (5) (2009) 350–358, https://doi.org/10.1002/adem.200800319.
[12] T. Tanaka, T. Morishige, T. Hirata, Comprehensive analysis of joint strength for dissimilar friction stir welds of mild steel to aluminum alloys, Scripta Mater. 61 (7) (2009) 756–759, https://doi.org/10.1016/j.scriptamat.2009.06.022.
[13] H. Springer, A. Kostka, J. Dos Santos, D. Raabe, Influence of intermetallic phases and Kirkendall-porosity on the mechanical properties of joints between steel and aluminium alloys, Mater. Sci. Eng. 528 (13–14) (2011) 4630–4642, https://doi.org/10.1016/j.msea.2011.02.057.
[14] R. Hatano, T. Ogura, T. Matsuda, T. Sano, A. Hirose, Relationship between intermetallic compound layer thickness with deviation and interfacial strength for dissimilar joints of aluminum alloy and stainless steel, Mater. Sci. Eng. 735 (2018) 361–366, https://doi.org/10.1016/j.msea.2018.08.065.
[15] S.M. Arbo, T. Bergh, H. Solhaug, I. Westermann, B. Holmedal, Influence of thermomechanical processing sequence on properties of AA6082-IF steel cold roll bonded composite sheet, Procedia Manuf 15 (2018) 152–160, https://doi.org/10.1016/j.promfg.2018.07.189.
[16] Ø. Grong, L. Sandnes, T. Bergh, P.E. Vullum, R. Holmestad, F. Berto, An analytical framework for modelling intermetallic compound (IMC) formation and optimising bond strength in aluminium-steel welds, Mater. Des. Process. Commun. 1 (2019) e57, https://doi.org/10.1002/mdp2.57.
[17] H. He, C. Wu, S. Lin, C. Yang, Pulsed TIG welding–brazing of aluminum–stainless steel with an Al-Cu twin hot wire, J. Mater. Eng. Perform. 28 (2) (2019) 1180–1189, https://doi.org/10.1007/s11665-018-3848-y.
[18] Y. Chen, Z. Yang, C. Shi, Z. Xin, Z. Zeng, Laser-CMT hybrid welding-brazing of Al/steel butt joint: weld formation, intermetallic compounds, and mechanical properties, Mater 12 (22) (2019) 3651, https://doi.org/10.3390/ma12223651.
[19] W.H. Jiang, R. Kovacevic, Feasibility study of friction stir welding of 6061-T6 aluminium alloy with AISI 1018 steel, Proc. Inst. Mech. Eng., Part B: J. Eng. Manuf. 218 (10) (2004) 1323–1331, https://doi.org/10.1243/0954405042323612.
[20] T. Chen, Process parameters study on FSW joint of dissimilar metals for aluminum–steel, J. Mater. Sci. 44 (10) (2009) 2573–2580, https://doi.org/10.1007/s10853-009-3336-8.
[21] M.K. Karfoul, G.J. Tatlock, R.T. Murray, The behaviour of iron and aluminium during the diffusion welding of carbon steel to aluminium, J. Mater. Sci. 42 (14) (2007) 5692–5699, https://doi.org/10.1007/s10853-006-0742-z.

[22] P. Prangnell, F. Haddadi, Y. Chen, Ultrasonic spot welding of aluminium to steel for automotive applications—microstructure and optimisation, Mater. Sci. Technol. 27 (3) (2011) 617–624, https://doi.org/10.1179/026708310X520484.

[23] H. Yu, Z. Xu, Z. Fan, Z. Zhao, C. Li, Mechanical property and microstructure of aluminum alloy-steel tubes joint by magnetic pulse welding, Mater. Sci. Eng. 561 (2013) 259–265, https://doi.org/10.1016/j.msea.2012.11.015.

[24] M. Pouranvari, Critical assessment 27: dissimilar resistance spot welding of aluminium/steel: challenges and opportunities, Mater. Sci. Technol. 33 (15) (2017) 1705–1712, https://doi.org/10.1080/02670836.2017.1334310.

[25] M. Movahedi, A. Kokabi, S.S. Reihani, H. Najafi, Effect of tool travel and rotation speeds on weld zone defects and joint strength of aluminium steel lap joints made by friction stir welding, Sci. Technol. Weld. Join. 17 (2) (2012) 162–167, https://doi.org/10.1179/1362171811Y.0000000092.

[26] W. Ratanathavorn, A. Melander, H. Magnusson, Intermetallic compounds in friction stirred lap joints between AA5754/galvanised ultra-high strength steel, Sci. Technol. Weld. Join. 21 (8) (2016) 653–659, https://doi.org/10.1080/13621718.2016.1163878.

[27] A. Simar, M.-N. Avettand-Fènoël, State of the art about dissimilar metal friction stir welding, Sci. Technol. Weld. Join. 22 (5) (2017) 389–403, https://doi.org/10.1080/13621718.2016.1251712.

[28] H. Durmuş, Consideration of cold metal transfer welding of AA5754 to galvanized steel from mechanical and microstructural aspects, Rev. Metal. (Madr.) 54 (1) (2018) e115, https://doi.org/10.3989/revmetalm.115.

[29] L. Zhou, M. Yu, B. Liu, Z. Zhang, S. Liu, X. Song, H. Zhao, Microstructure and mechanical properties of Al/steel dissimilar welds fabricated by friction surfacing assisted friction stir lap welding, J. Mater. Res. Technol. 9 (1) (2020) 212–221, https://doi.org/10.1016/j.jmrt.2019.10.046.

[30] S. Li, Y. Chen, J. Kang, B.S. Amirkhiz, F. Nadeau, Friction stir lap welding of aluminum alloy to advanced high strength steel using a cold-spray deposition as an interlayer, Mater. Lett. 239 (2019) 212–215, https://doi.org/10.1016/j.matlet.2018.12.060.

[31] C. Thomy, F. Vollertsen, Laser-MIG hybrid welding of aluminium to steel—effect of process parameters on joint properties, Weld. World 56 (5–6) (2012) 124–132, https://doi.org/10.1007/BF03321356.

[32] X. Fei, X. Jin, Y. Ye, T. Xiu, H. Yang, Effect of pre-hole offset on the property of the joint during laser-assisted friction stir welding of dissimilar metals steel and aluminum alloys, Mater. Sci. Eng. 653 (2016) 43–52, https://doi.org/10.1016/j.msea.2015.11.101.

[33] Y. Kusuda, Honda develops robotized FSW technology to weld steel and aluminum and applied it to a mass-production vehicle, Ind. Robot: Int. J. 40 (3) (2013) 208–212, https://doi.org/10.1108/01439911311309889.

[34] K. Furukawa, New CMT arc welding process–welding of steel to aluminium dissimilar metals and welding of super-thin aluminium sheets, Weld. Int. 20 (6) (2006) 440–445, https://doi.org/10.1533/wint.2006.3598.

[35] F. Berto, L. Sandnes, F. Abbatinali, Ø. Grong, P. Ferro, Using the hybrid metal extrusion & bonding (HYB) process for dissimilar joining of aa6082-T6 and S355, Procedia Struct. Integr. 13 (2018) 249–254, https://doi.org/10.1016/j.prostr.2018.12.042.

[36] Ø. Grong, L. Sandnes, F. Berto, A status report on the hybrid metal extrusion & bonding (HYB) process and its applications, Mater. Des. Process. Commun. 1 (2) (2019) e41, https://doi.org/10.1002/mdp2.41.

[37] Ø. Grong, L. Sandnes, F. Berto, Progress in solid state joining of metals and alloys, Procedia Struct. Integr. 17 (2019) 788–798, https://doi.org/10.1016/j.prostr.2019.08.105.

[38] L. Sandnes, L. Romere, F. Berto, T. Welo, Ø. Grong, Assessment of the mechanical integrity of a 2 mm aa6060-T6 butt weld produced using the hybrid metal extrusion & bonding (HYB) process –Part I: bend test results, Procedia Manuf 34 (2019) 147–153, https://doi.org/10.1016/j.promfg.2019.06.132.

[39] L. Sandnes, L. Romere, Ø. Grong, F. Berto, T. Welo, Assessment of the mechanical integrity of a 2 mm aa6060-T6 butt weld produced using the hybrid metal extrusion & bonding (HYB) process – Part II: tensile test results, Procedia Struct. Integr. 17 (2019) 632–642, https://doi.org/10.1016/j.prostr.2019.08.085.

[40] L. Sandnes, Ø. Grong, J. Torgersen, T. Welo, F. Berto, Exploring the hybrid metal extrusion and bonding process for butt welding of Al–Mg–Si alloys, Int. J. Adv. Manuf. Technol. 98 (5) (2018) 1059–1065, https://doi.org/10.1007/s00170-018-2234-0.

[41] Ø. Grong, Recent advances in solid-state joining of aluminum, Weld. J. 91 (1) (2012) 26–33.

[42] T. Bergh, L. Sandnes, D. Johnstone, P.A. Midgley, F. Berto, R. Holmestad, Ø. Grong, P.E. Vullum, Microstructural and mechanical characterisation of a hybrid metal extrusion & bonding aluminium-steel butt joint, Mater. Char. (2020), https://doi.org/10.1016/j.matchar.2020.110761.

[43] T. Watanabe, H. Takayama, A. Yanagisawa, Joining of aluminum alloy to steel by friction stir welding, J. Mater. Process. Technol. 178 (1) (2006) 342–349, https://doi.org/10.1016/j.jmatprotec.2006.04.117.

[44] A. Yazdipour, A. Heidarzadeh, Effect of friction stir welding on microstructure and mechanical properties of dissimilar Al 5083-H321 and 316L stainless steel alloy joints, J. Alloys Compd. 680 (2016) 595–603, https://doi.org/10.1016/j.jallcom.2016.03.307.

[45] M. Ghosh, R. Gupta, M. Husain, Friction stir welding of stainless steel to Al alloy: effect of thermal condition on weld nugget microstructure, Metall. Mater. Trans. 45 (2) (2014) 854–863, https://doi.org/10.1007/s11661-013-2036-9.

[46] H. Bang, H. Bang, G. Jeon, I. Oh, C. Ro, Gas tungsten arc welding assisted hybrid friction stir welding of dissimilar materials Al6061-T6 aluminum alloy and STS304 stainless steel, Mater. Des. 37 (2012) 48–55, https://doi.org/10.1016/j.matdes.2011.12.018.

[47] R. Coelho, A. Kostka, J. Dos Santos, A. Kaysser-Pyzalla, Friction-stir dissimilar welding of aluminium alloy to high strength steels: mechanical properties and their relation to microstructure, Mater. Sci. Eng. 556 (2012) 175–183, https://doi.org/10.1016/j.msea.2012.06.076.

[48] S. Zhao, J. Ni, G. Wang, Y. Wang, Q. Bi, Y. Zhao, X. Liu, Effects of tool geometry on friction stir welding of AA6061 to TRIP steel, J. Mater. Process. Technol. 261 (2018) 39–49, https://doi.org/10.1016/j.jmatprotec.2018.06.003.

[49] S. Lan, X. Liu, J. Ni, Microstructural evolution during friction stir welding of dissimilar aluminum alloy to advanced high-strength steel, Int. J. Adv. Manuf. Technol. 82 (9–12) (2016) 2183–2193, https://doi.org/10.1007/s00170-015-7531-2.

[50] F. Leoni, Ø. Grong, L. Sandnes, T. Welo, F. Berto, Finite element modelling of the filler wire feeding in the hybrid metal extrusion & bonding (HYB) process, J. Adv. Join. Process. 1 (2020), 100006, https://doi.org/10.1016/j.jajp.2020.100006.

[51] J.E. Hatch, Aluminum: Properties and Physical Metallurgy, American Society for Metals, Materials Park, Ohio (US), 1984.

[52] ASTM E92-16, Standard Test Methods for Vickers Hardness and Knoop Hardness of Metallic Materials, ASTM International, West Conshohocken, PA, 2016.

[53] HyperSpy v1.5.2. https://zenodo.org/record/3396791#.Xpg37kczaUl, 2019 accessed 21 January 2021.

[54] ASTM E8/E8M-16a, Standard Test Methods for Tension Testing of Metallic Materials, ASTM International, West Conshohocken, 2016.

[55] E. Fagerholt, T. Børvik, O.S. Hopperstad, Measuring discontinuous displacement fields in cracked specimens using digital image correlation with mesh adaptation and crack-path optimization, Optic Laser. Eng. 51 (3) (2013) 299–310, https://doi.org/10.1016/j.optlaseng.2012.09.010.

[56] E. Fagerholt, E. Østby, T. Børvik, O.S. Hopperstad, Investigation of fracture in small-scale SENT tests of a welded X80 pipeline steel using Digital Image Correlation with node splitting, Eng. Fract. Mech. 96 (2012) 276–293, https://doi.org/10.1016/j.engfracmech.2012.08.007.

[57] U.R. Aakenes, Ø. Grong, T. Austigard, Application of the hybrid metal extrusion & bonding (HYB) method for joining of AA6082-T6 base material, Mater. Sci. Forum 794 (2014) 339–344. https://doi.org/10.4028/www.scientific.net/MSF.794-796.339.

[58] K. Wang, P. Upadhyay, Y. Wang, J. Li, X. Sun, T. Roosendaal, Investigation of interfacial layer for friction stir scribe welded aluminum to steel joints, J. Manuf. Sci. Eng. 140 (11) (2018), https://doi.org/10.1115/1.4040873.

[59] P. Upadhyay, Y. Hovanski, S. Jana, L.S. Fifield, Joining dissimilar materials using friction stir scribe technique, J. Manuf. Sci. Eng. 139 (3) (2017), https://doi.org/10.1115/1.4034629.

[60] N. Krendelsberger, F. Weitzer, J.C. Schuster, On the reaction scheme and liquidus surface in the ternary system Al-Fe-Si, Metall. Mater. Trans. 38 (8) (2007) 1681–1691, https://doi.org/10.1007/s11661-007-9182-x.

[61] M.C. Marker, B. Skolyszewska-Kühberger, H.S. Effenberger, C. Schmetterer, K. W. Richter, Phase equilibria and structural investigations in the system Al–Fe–Si, Intermet 19 (12) (2011) 1919–1929, https://doi.org/10.1016/j.intermet.2011.05.003.

[62] M. Cooper, The crystal structure of the ternary alloy α (AlFeSi), Acta Crystallogr. 23 (6) (1967) 1106–1107, https://doi.org/10.1107/S0365110X67004372.

[63] H. Springer, A. Kostka, E. Payton, D. Raabe, A. Kaysser-Pyzalla, G. Eggeler, On the formation and growth of intermetallic phases during interdiffusion between low-carbon steel and aluminum alloys, Acta Mater. 59 (4) (2011) 1586–1600, https://doi.org/10.1016/j.actamat.2010.11.023.

[64] W.-J. Cheng, C.-J. Wang, Observation of high-temperature phase transformation in the Si-modified aluminide coating on mild steel using EBSD, Mater. Char. 61 (4) (2010) 467–473, https://doi.org/10.1016/j.matchar.2010.02.001.

[65] S. Kundu, D. Roy, R. Bhola, D. Bhattacharjee, B. Mishra, S. Chatterjee, Microstructure and tensile strength of friction stir welded joints between interstitial free steel and commercially pure aluminium, Mater. Des. 50 (2013) 370–375, https://doi.org/10.1016/j.matdes.2013.02.017.

[66] S. Bozzi, A.L. Helbert-Etter, T. Baudin, B. Criqui, J.G. Kerbiguet, Intermetallic compounds in Al 6016/IF-steel friction stir spot welds, Mater. Sci. Eng. 527 (16) (2010) 4505–4509, https://doi.org/10.1016/j.msea.2010.03.097.

[67] M. Dehghani, A. Amadeh, S.A.A. Akbari Mousavi, Investigations on the effects of friction stir welding parameters on intermetallic and defect formation in joining aluminum alloy to mild steel, Mater. Des. 49 (2013) 433–441, https://doi.org/10.1016/j.matdes.2013.01.013.

[68] P. Karakizis, D. Pantelis, D. Dragatogiannis, V. Bougiouri, C. Charitidis, Study of friction stir butt welding between thin plates of AA5754 and mild steel for automotive applications, Int. J. Adv. Manuf. Technol. 102 (9–12) (2019) 3065–3076, https://doi.org/10.1007/s00170-019-03388-9.

[69] M. Yılmaz, M. Çöl, M. Acet, Interface properties of aluminum/steel friction-welded components, Mater. Char. 49 (5) (2002) 421–429, https://doi.org/10.1016/S1044-5803(03)00051-2.

[70] K. Ramachandran, N. Murugan, S.S. Kumar, Effect of tool axis offset and geometry of tool pin profile on the characteristics of friction stir welded dissimilar joints of aluminum alloy AA5052 and HSLA steel, Mater. Sci. Eng. 639 (2015) 219–233, https://doi.org/10.1016/j.msea.2015.04.089.

[71] W.-B. Lee, M. Schmuecker, U.A. Mercardo, G. Biallas, S.-B. Jung, Interfacial reaction in steel–aluminum joints made by friction stir welding, Scripta Mater. 55 (4) (2006) 355–358, https://doi.org/10.1016/j.scriptamat.2006.04.028.

[72] X. Liu, S. Lan, J. Ni, Analysis of process parameters effects on friction stir welding of dissimilar aluminum alloy to advanced high strength steel, Mater. Des. 59 (2014) 50–62, https://doi.org/10.1016/j.matdes.2014.02.003.

[73] X. Liu, S. Lan, J. Ni, Electrically assisted friction stir welding for joining Al 6061 to TRIP 780 steel, J. Mater. Process. Technol. 219 (2015) 112–123, https://doi.org/10.1016/j.jmatprotec.2014.12.002.
[74] Z. Lu, W. Gong, S. Chen, T. Yuan, C. Kan, X. Jiang, Interfacial microstructure and local bonding strength of magnetic pulse welding joint between commercially pure aluminum 1060 and AISI 304 stainless steel, J. Manuf. Process. 46 (2019) 59–66, https://doi.org/10.1016/j.jmapro.2019.07.041.
[75] Ø. Grong, Metallurgical Modelling of Welding, Institute of Materials, Cambridge (UK), 1997.
[76] N.E. Dowling, R. Narayanasamy, K.S. Prasad, Mechanical Behavior of Materials: Engineering Methods for Deformation, Fracture, and Fatigue, fourth ed., Pearson Education, Edinburgh, England, 2013.
[77] G. Qin, Y. Ji, H. Ma, Z. Ao, Effect of modified flux on MIG arc brazing-fusion welding of aluminum alloy to steel butt joint, J. Mater. Process. Technol. 245 (2017) 115–121, https://doi.org/10.1016/j.jmatprotec.2017.02.022.
[78] H. Xia, X. Zhao, C. Tan, B. Chen, X. Song, L. Li, Effect of Si content on the interfacial reactions in laser welded-brazed Al/steel dissimilar butted joint, J. Mater. Process. Technol. 258 (2018) 9–21, https://doi.org/10.1016/j.jmatprotec.2018.03.010.
[79] L. Li, H. Xia, C. Tan, N. Ma, Influence of laser power on interfacial microstructure and mechanical properties of laser welded-brazed Al/steel dissimilar butted joint, J. Manuf. Process. 32 (2018) 160–174, https://doi.org/10.1016/j.jmapro.2018.02.002.
[80] M. Zhang, G. Chen, Y. Zhang, K. Wu, Research on microstructure and mechanical properties of laser keyhole welding–brazing of automotive galvanized steel to aluminum alloy, Mater. Des. 45 (2013) 24–30, https://doi.org/10.1016/j.matdes.2012.09.023.
[81] Y. Meng, M. Gong, S. Zhang, Y. Zhang, M. Gao, Effects of oscillating laser offset on microstructure and properties of dissimilar Al/steel butt-joint, Optic Laser. Eng. 128 (2020), 106037, https://doi.org/10.1016/j.optlaseng.2020.106037.
[82] L. Li, H. Xia, C. Tan, N. Ma, Effect of groove shape on laser welding-brazing Al to steel, J. Mater. Process. Technol. 252 (2018) 573–581, https://doi.org/10.1016/j.jmatprotec.2017.10.025.
[83] J. Xue, Y. Li, H. Chen, Z. Zhu, Effects of heat input on wettability, interface microstructure and properties of Al/steel butt joint in laser-metal inert-gas hybrid welding-brazing, J. Mater. Process. Technol. 255 (2018) 47–54, https://doi.org/10.1016/j.jmatprotec.2017.11.063.
[84] S. Chen, S. Li, Y. Li, J. Huang, S. Chen, J. Yang, Butt welding-brazing of steel to aluminum by hybrid laser-CMT, J. Mater. Process. Technol. 272 (2019) 163–169, https://doi.org/10.1016/j.jmatprotec.2019.05.018.
[85] T. Yasui, M. Tsubaki, M. Fukumoto, Y. Shimoda, T. Ishii, High-speed weldability between 6063 and S45C by friction stir welding. Study of welding of dissimilar metals by friction stir welding (1st report), Weld. Int. 20 (4) (2006) 284–289, https://doi.org/10.1533/wint.2006.3580.